Hair cells use active zones with different voltage dependence of Ca^{2+} influx to decompose sounds into complementary neural codes

Tzu-Lun Ohn[a,b,c,d], Mark A. Rutherford[a,e,1], Zhizi Jing[b,d,f,1], Sangyong Jung[a,g,h,1], Carlos J. Duque-Afonso[a,b], Gerhard Hoch[a], Maria Magdalena Picher[a,b], Anja Scharinger[i,j], Nicola Strenzke[b,d,f], and Tobias Moser[a,b,c,d,g,h,k,2]

[a]Institute for Auditory Neuroscience & InnerEarLab, University Medical Center Göttingen, 37099 Goettingen, Germany; [b]Göttingen Graduate School for Neurosciences and Molecular Biosciences, University of Göttingen, 37073 Goettingen, Germany; [c]Bernstein Focus for Neurotechnology, University of Göttingen, 37073 Goettingen, Germany; [d]Collaborative Research Center 889, University of Göttingen, 37099 Goettingen, Germany; [e]Department of Otolaryngology, Washington University School of Medicine, St. Louis, MO 63110; [f]Auditory Systems Physiology Group, InnerEarLab, Department of Otolaryngology, University Medical Center Göttingen, 37099 Goettingen, Germany; [g]Synaptic Nanophysiology Group, Max Planck Institute for Biophysical Chemistry, 37077 Goettingen, Germany; [h]Center for Nanoscale Microscopy and Molecular Physiology of the Brain, University of Göttingen, 37073 Goettingen, Germany; [i]Institute of Pharmacy, Department of Pharmacology and Toxicology, University of Innsbruck, A-6020 Innsbruck, Austria; [j]Center for Chemistry and Biomedicine, University of Innsbruck, A-6020 Innsbruck, Austria; and [k]Bernstein Center for Computational Neuroscience, University of Göttingen, 37073 Goettingen, Germany

Edited by A. J. Hudspeth, The Rockefeller University, New York, NY, and approved June 21, 2016 (received for review April 8, 2016)

For sounds of a given frequency, spiral ganglion neurons (SGNs) with different thresholds and dynamic ranges collectively encode the wide range of audible sound pressures. Heterogeneity of synapses between inner hair cells (IHCs) and SGNs is an attractive candidate mechanism for generating complementary neural codes covering the entire dynamic range. Here, we quantified active zone (AZ) properties as a function of AZ position within mouse IHCs by combining patch clamp and imaging of presynaptic Ca^{2+} influx and by immunohistochemistry. We report substantial AZ heterogeneity whereby the voltage of half-maximal activation of Ca^{2+} influx ranged over ∼20 mV. Ca^{2+} influx at AZs facing away from the ganglion activated at weaker depolarizations. Estimates of AZ size and Ca^{2+} channel number were correlated and larger when AZs faced the ganglion. Disruption of the deafness gene *GIPC3* in mice shifted the activation of presynaptic Ca^{2+} influx to more hyperpolarized potentials and increased the spontaneous SGN discharge. Moreover, *Gipc3* disruption enhanced Ca^{2+} influx and exocytosis in IHCs, reversed the spatial gradient of maximal Ca^{2+} influx in IHCs, and increased the maximal firing rate of SGNs at sound onset. We propose that IHCs diversify Ca^{2+} channel properties among AZs and thereby contribute to decomposing auditory information into complementary representations in SGNs.

auditory system | spiral ganglion neuron | dynamic range | synaptic strength | presynaptic heterogeneity

The auditory system enables us to perceive sound pressures that vary over six orders of magnitude. This is achieved by active amplification of cochlear vibrations at low sound pressures and compression at high sound pressures. The receptor potential of inner hair cells (IHCs) represents the full range (1), whereas each postsynaptic type I spiral ganglion neuron (hereafter termed SGN) encodes only a fraction (2–6). SGNs with comparable frequency tuning but different spontaneous spike rates and sound responses are thought to emanate from neighboring, if not the same, IHC at a given tonotopic position of the organ of Corti (2, 5, 7, 8). Even in silence, IHC active zones (AZs) release glutamate at varying rates, evoking "spontaneous" spiking in SGNs. SGNs with greater spontaneous spike rates respond to softer sounds (high-spontaneous rate, low-threshold SGNs), than those with lower spontaneous spike rates (low-spontaneous rate, high-threshold SGNs) (2, 9). This diversity likely underlies the representation of sounds across all audible sound pressure levels in the auditory nerve, to which neural adaptation also contributes (10).

How SGN diversity arises is poorly understood. Candidate mechanisms include the heterogeneity of ribbon synapses that differ in pre- and/or postsynaptic properties even within individual IHCs (7, 11–14). IHC AZs vary in the number (11, 15) and voltage dependence of gating (11) of their Ca^{2+} channels regardless of tonotopic position (16). Lateral olivocochlear efferent projections to the SGNs regulate postsynaptic excitability (17) and contribute to the establishment of a gradient of presynaptic ribbon size along the "modiolar–pillar" axis (18), where the modiolar side faces the ganglion and the pillar side is away from the ganglion, toward the pillar cells.

In postnatal development of the mouse, high-spontaneous-rate SGNs coemerge with AZs that exhibit stronger maximal Ca^{2+} influx. Moreover, IHCs deficient for the AZ protein bassoon lack the population of AZs with strongest Ca^{2+} influx and, concurrently lack SGNs with high spontaneous rates (19). Based on these correlations and given the eminent role of presynaptic Ca^{2+} influx in controlling synaptic strength (20–22), we proposed that the varying Ca^{2+} influx at a given IHC AZ largely determines the difference in spontaneous and evoked spiking among SGNs (19). Larger and more complex AZs (7, 13, 14) with stronger Ca^{2+} influx (16) tend to reside on the modiolar IHC side. However, according to classical findings from the cat cochlea, modiolar synapses seem weaker as they drive

Significance

We hear sounds varying in intensity over six orders of magnitude using spiral ganglion neurons (SGNs), each of which changes its firing rates over only a fraction of this range. Somehow, the SGNs with different dynamic ranges collectively encode the full range of sound levels represented in the receptor potential of the inner hair cell (IHC) in the mammalian cochlea. Our study, combining subcellular imaging, mouse genetics, and auditory systems physiology, offers a unifying synaptic hypothesis for wide dynamic range sound encoding in the spiral ganglion. We propose that IHCs, from one receptor potential but via presynaptic active zones that vary in the voltage dependence of Ca^{2+} influx, generate complementary codes on sound pressure level in functionally distinct SGNs.

Author contributions: T.M. designed research; T.-L.O., M.A.R., Z.J., S.J., C.J.D.-A., and M.M.P. performed research; G.H. and A.S. contributed new reagents/analytic tools; T.-L.O., M.A.R., Z.J., S.J., C.J.D.-A., and N.S. analyzed data; and T.-L.O., M.A.R., Z.J., S.J., C.J.D.-A., M.M.P., N.S., and T.M. wrote the paper.

The authors declare no conflict of interest.

This article is a PNAS Direct Submission.

[1]M.A.R., Z.J., and S.J. contributed equally to this work.

[2]To whom correspondence should be addressed. Email: tmoser@gwdg.de.

This article contains supporting information online at www.pnas.org/lookup/suppl/doi:10.1073/pnas.1605737113/-/DCSupplemental.

low-spontaneous-rate, high-threshold SGNs (2, 7). This discrepancy suggests that factors other than AZ size and amplitude of Ca^{2+} influx contribute to differences in SGN properties.

Here, we live-imaged most, if not all, AZs of individual IHCs for analyzing the amplitude and voltage dependence of Ca^{2+} influx as well as AZ size and position within the IHC. Combined with immunohistochemical estimation of ribbon size and Ca^{2+}-channel abundance of AZs, our data indicate opposing gradients of maximal amplitude and voltage dependence of Ca^{2+} influx along the modiolar–pillar axis: modiolar AZs, thought to drive low-spontaneous-rate, high-threshold SGNs, are, on average, larger and have more Ca^{2+} channels but operate in a more depolarized range. We propose that the more hyperpolarized activation range of Ca^{2+} influx at pillar AZs poises them to enable high spontaneous rates and low sound thresholds of SGN firing. We studied candidate regulators of Ca^{2+} influx at IHC AZs and found that disruption of the deafness gene *GIPC3* in mice causes a hyperpolarizing shift of Ca^{2+}-channel activation and increases spontaneous SGN firing.

Results

Heterogeneity of Presynaptic Ca^{2+} Influx Among the AZs of IHCs. The strength of presynaptic Ca^{2+} influx and the large (~2 μm) distance between hair cell AZs (16, 23) enable spatiotemporally resolved optical analysis of presynaptic Ca^{2+} signaling (11, 24, 25). However, given the limited duration of stable Ca^{2+} influx in whole-cell patch-clamp recordings, the low speed of laser-scanning confocal microscopy had prohibited a comprehensive comparison of the Ca^{2+}-influx properties among the AZs within a given IHC. To overcome this technical limitation we combined spinning disk microscopy with fast piezoelectric focusing to sequentially and rapidly (frame rate 100 Hz) image confocal IHC sections. This enabled the analysis of voltage dependence and maximal amplitude of the Ca^{2+} influx, visualized as local fluorescence increase of the low-affinity Ca^{2+} indicator Fluo-8FF (K_d = 10 μM) at most if not all synapses of a given IHC (Fig. 1*A*) while the IHC Ca^{2+} current remained stable (rundown <25%; a few IHCs were excluded from the analysis because of rundown >25%).

We first imaged the fluorescence of the TAMRA (tetramethylrhodamine)-labeled RIBEYE (major protein constituent of the ribbon)-binding peptide (26) to localize AZs and to measure the fluorescence intensity of labeled ribbons before unavoidable TAMRA bleaching by the strong blue laser light used for Ca^{2+} imaging. Another set of images was collected after completing the time-critical Ca^{2+} imaging to capture IHC morphology based on the RIBEYE-peptide background fluorescence (Fig. 1*A*). Supported by our previous work we assume that, in conditions of strong cytosolic Ca^{2+} buffering (10 mM EGTA in the pipette), the fluorescence change ($\Delta F/F_0$, Fig. 1*B*) of the low-affinity Ca^{2+} indicator at the AZ faithfully reports synaptic Ca^{2+} influx (11), but note that this assumption could be violated should Ca^{2+}-indicator saturation or Ca^{2+}-induced Ca^{2+} release, nonetheless, occur. For simplicity, we hence refer to the Fluo-8FF $\Delta F/F_0$ at AZs as "synaptic Ca^{2+} influx." We depolarized the IHC to −7 mV to maximize Ca^{2+}-channel-open probability. As shown in Fig. 1*B*, the "maximal synaptic Ca^{2+} influx" varied among the AZs of this representative IHC, whereas the whole-cell Ca^{2+} current remained stable. We postulate that this heterogeneity largely arises from differences in the number of Ca^{2+} channels among the AZs within a given IHC. The coefficient of variation (c.v.) of maximal AZ Ca^{2+} influx per IHC was on average similar to the c.v. of maximal AZ Ca^{2+} influx across AZ pooled from all IHCs (c.v. = 0.47 ± 0.18, N = 28 IHCs vs. c.v.= 0.59, n = 331 AZs of the same 28 IHCs; Fig. 1 *D* and *F*), whereas the c.v. of maximal AZ Ca^{2+} influx across all IHCs was smaller (0.38). Thus, most of the AZ population variance was explained by heterogeneity among the AZs within the individual IHCs. However, IHCs varied in the extent of this heterogeneity: The c.v. of maximal Ca^{2+} influx among AZs per IHC ranged from 0.15 to 0.81 (Fig. 1*F*; see Fig. S1*A* for statistics of individual IHCs).

We directly tested for heterogeneous abundance of Ca^{2+} channels at AZs by analyzing the relative fluorescence intensities of IHC AZs immunolabeled for $Ca_V1.3$ L-type Ca^{2+} channels (Fig. 1 *C* and *D*, blue), which mediate >90% of IHC Ca^{2+} influx (27, 28). To measure the relative abundance of $Ca_V1.3$ Ca^{2+} channels among AZs, we identified synapses in fixed tissue by juxtaposition of immunolabeled presynaptic ribbons and postsynaptic glutamate receptors (Fig. 1*C*) and integrated the synaptic $Ca_V1.3$ immunofluorescence. Interestingly, the variability of the synaptic $Ca_V1.3$ immunofluorescence was smaller (c.v. = 0.28) than that of maximal Ca^{2+} influx in live-cell imaging experiments (c.v. = 0.59, Fig. 1*D*; see statistics of individual cells in Fig. S1 *A* and *B*). Variance in maximal Ca^{2+} influx exceeding that of $Ca_V1.3$ immunofluorescence could be explained, for example, by AZs having $Ca_V1.3$ channels with different open probabilities.

Ca^{2+}-Channel Abundance and Maximal Ca^{2+} Influx Scale with Ribbon Size. Do larger AZs contain more Ca^{2+} channels and display stronger maximal Ca^{2+} influx? To address this, we related our estimates of Ca^{2+}-channel abundance from live imaging and immunohistochemistry to the corresponding fluorescence intensity of RIBEYE-peptide or immunolabeled ribbons (Fig. 1 *A* and *C*; see statistics of individual cells in Fig. S1 *A* and *B*). We assume that ribbon fluorescence scales with the number of RIBEYE molecules per ribbon and, hence, with ribbon size (26, 29). Moreover, we assume that AZ size scales with ribbon size (29, 30), which was further supported by a positive correlation of synaptic immunofluorescence of RIBEYE and the AZ marker bassoon, a presynaptic scaffold, in separate experiments (r = 0.46, n = 77 AZs, P < 0.001). The distributions of ribbon fluorescence intensity were broad and slightly skewed in live imaging (Fig. 1 *E* and *F*; c.v. of 0.46 for the entire population and 0.31 as the mean c.v. of individual cells, Fig. S1*D*) and immunofluorescence (c.v. of 0.46 for the entire population and 0.42 as the mean c.v. of individual cells) analyses, respectively.

Maximal AZ Ca^{2+} influx showed a positive correlation with the RIBEYE-peptide fluorescence in live-imaging experiments, suggesting that, indeed, larger AZs exhibit stronger maximal Ca^{2+} influx (Fig. 1*G*, green). We found a stronger correlation between $Ca_V1.3$ and RIBEYE immunofluorescence (Fig. 1*G*, blue), indicating that larger AZs contain more Ca^{2+} channels. This weaker correlation in live imaging might relate to greater variability of maximal synaptic Ca^{2+} influx, which next to the number of Ca^{2+} channels depends on their open probability that can also be enhanced by calmodulin-mediated cooperative gating (31). Positive correlations were also found within most individual IHCs in both live-cell imaging and immunohistochemistry (Fig. S1 *D* and *E*), indicating that larger AZs tended to have more Ca^{2+} channels and, consequently, stronger maximal Ca^{2+} influx. This was further supported by finding a positive correlation of synaptic $Ca_V1.3$ and bassoon immunofluorescence in separate experiments (Fig. S1*C*, r = 0.625, n = 77 AZs, P < 0.001). Most cells contained an AZ whose Ca^{2+} influx was substantially stronger than that of the others: On average the $\Delta F/F_0$ of the strongest AZ ("winner") was 2.5 times greater than the average of the others (Fig. S1*F*, P < 0.001, Wilcoxon rank sum test).

Maximal Ca^{2+} Influx Varies with AZ Position in a Modiolar–Pillar Gradient. To study whether structural and functional AZ properties vary with position in mouse IHCs, we maintained the native morphology and position of the IHC within the organ of Corti as much as possible, by patching the modiolar IHC face with minimal disruption of the surrounding cells. To combine live-imaging data from several cells, we reconstructed the morphology of individual IHCs and the positions of their synapses based on the fluorescence of the TAMRA-conjugated RIBEYE-binding peptide and then

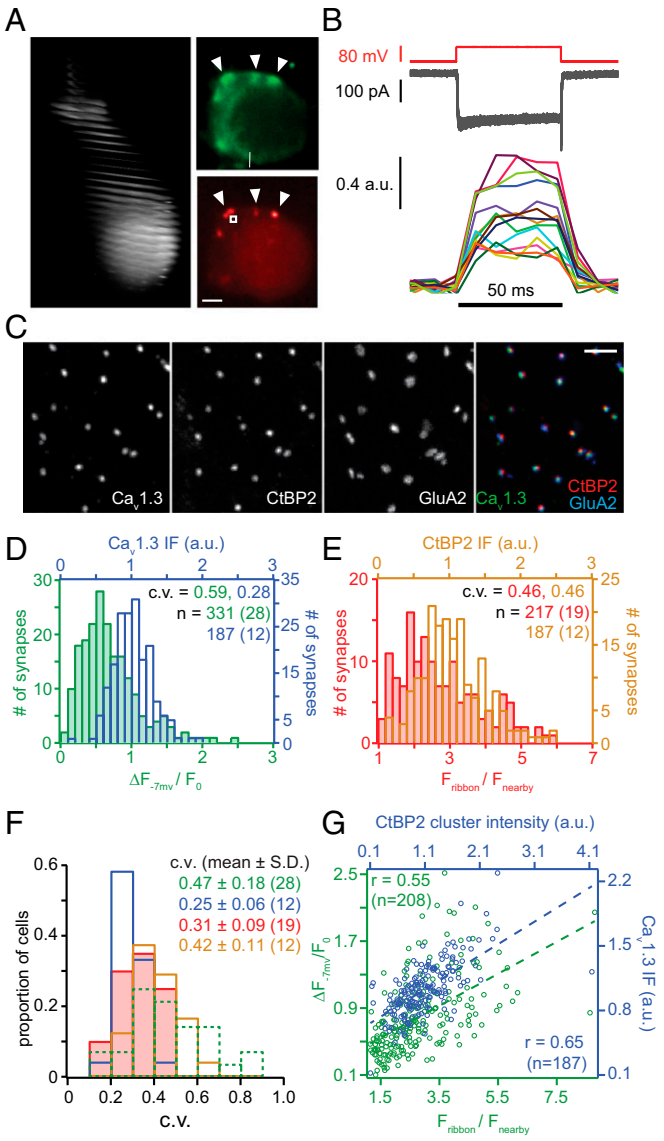

Fig. 1. AZ heterogeneity: Those with larger ribbons have more Ca^{2+} channels. (*A*, *Left*) Stack of confocal sections covering an exemplary IHC filled with TAMRA-RIBEYE-binding peptide via the patch pipette. (*A*, *Upper Right*) Fluo-8FF fluorescence reports Ca^{2+} influx (arrowheads) as spot-like maxima near the membrane during depolarization. (*A*, *Lower Right*) Corresponding image of TAMRA-RIBEYE-binding peptide fluorescence labeling synaptic ribbons (arrowheads), where Ca^{2+} influx occurs. White square indicates where the background fluorescence (F_{nearby}) was measured. (Scale bar: 1 μm.) (*B*) Measurement of Ca^{2+} influx at individual AZs in an exemplary IHC. Depolarizations to −7 mV (*Upper*) evoked similar whole-cell Ca^{2+} currents with each stimulus (superimposed, *Middle*). Focusing on single AZs during each repetition revealed major heterogeneity of maximal Ca^{2+}-indicator fluorescence amplitudes (*Lower*, $\Delta F_{-7\ mV}/F_0$, 100-Hz frame rate; panel superimposes one trace per AZ, each marked by a different color). (*C*) Confocal projections of immunolabeled presynaptic Ca^{2+} channels ($Ca_v1.3$), presynaptic ribbons (CtBP2/RIBEYE), and postsynaptic AMPA receptors (GluA2) with overlay on far right. (Scale bar: 2 μm.) (*D*) Green: distribution of the maximal $\Delta F_{-7\ mV}/F_0$ for each AZ from live imaging. Blue: distribution of the integrated $Ca_v1.3$ immunofluorescence pixel intensities for each AZ in fixed tissue. (*E*) Red: distribution of the maximal fluorescence intensity of TAMRA-peptide labeled ribbons, normalized to the cytosolic fluorescence (F_{ribbon}/F_{nearby}). Brown: distribution of the integrated CtBP2/RIBEYE immunofluorescence pixel intensites for each AZ. (*F*) Distributions of the c.v. estimated within individual IHCs for AZ parameters: maximal Ca^{2+} influx ($\Delta F_{-7\ mV}/F_0$, dashed green), TAMRA-RIBEYE-binding peptide fluorescence (solid red), $Ca_v1.3$ immunofluorescence (solid blue), and CtBP2/RIBEYE immunofluorescence (solid brown). (*G*) Scatter plot of maximal $\Delta F_{-7\ mV}/F_0$ vs. TAMRA-RIBEYE-binding fluorescence intensity (green) and of $Ca_v1.3$ vs. CtBP2/RIBEYE immunofluorescence (blue). Dashed lines are linear regressions and r is Pearson's correlation coefficient.

transformed the Cartesian coordinates onto cell-aligned cylindrical coordinates (Fig. S2). In brief, for each cell we identified the plane of maximized mirror symmetry orthogonal to the tonotopic axis (Fig. S2*A*). Then, we optically resectioned the IHC orthogonal to a straight line fit to the pillar edge of the plane of symmetry (Fig. S2*B*). We estimated the center of mass for each section and connected those of the bottom-most and of the largest section to define the central axis for our cylindrical coordinate system. We projected the AZ coordinates of several cells along their central axis for the polar charts, with the four sides annotated as modiolar or pillar (facing toward or away from the ganglion), or tonotopic-apical or tonotopic-basal (toward the cochlear apex or base, Fig. S2*C*). The analogous fixed-tissue volumes were also transformed into cylindrical coordinates (Fig. S3).

Polar charts of maximal Ca^{2+} influx and ribbon size for 202 AZs from 14 IHCs as a function of AZ cylindrical coordinates are displayed in Fig. 2 *A* and *B*. Our analysis revealed a modiolar–pillar gradient: large AZs with stronger Ca^{2+} influx tended toward the modiolar face (Fig. 2 *A*–*D*, *F*, and *G*). There was a nonsignificant trend for maximal Ca^{2+} influx to be greater in the modiolar half of the AZ population. This difference became significant when excluding the AZs of the basal IHC pole ($r \leq 3$ μm, Fig. S4*A*, $P = 0.024$, Wilcoxon rank sum test), for which modiolar/pillar sorting is less certain. In 13 out of 14 IHCs the AZ with the strongest Ca^{2+} influx was located on the modiolar side. $Ca_V1.3$ immunofluorescence was significantly more intense for modiolar AZs (Fig. 2 *C* and *E*, $P < 0.001$, Wilcoxon rank sum test). RIBEYE-peptide ribbon fluorescence (Fig. 2 *B*, *F*, and *G*, $P < 0.05$, Wilcoxon rank sum test) and RIBEYE immunofluorescence (Fig. 2 *F* and *H*, $P < 0.01$, Wilcoxon rank sum test) consistently revealed significant modiolar–pillar differences, indicating that modiolar AZs are larger. In contrast, we did not detect gradients along the tonotopic or the central axes of the IHCs for any of the analyzed parameters (Fig. S4 *B* and *C*). In conclusion, IHC AZs follow a modiolar–pillar gradient for size and Ca^{2+}-channel number, whereby modiolar AZs are larger and have more Ca^{2+} channels.

Voltage Dependence of Ca^{2+} Influx Varies with AZ Position in a Pillar–Modiolar Gradient. Next, we examined the voltage dependence of synaptic Ca^{2+} influx for most if not all AZs of a given IHC. We applied voltage ramps (from −87 mV to 63 mV) to the IHC while sequentially imaging the AZs (Fig. 3*A*), thereby establishing the voltage dependence of AZ Ca^{2+} influx in single depolarizations. Using ramps instead of step depolarizations, we limited stimulation to at most 80 depolarizations per IHC. We estimated the voltage of half-maximal activation of the whole-cell Ca^{2+} current of 25 IHCs by fitting a Boltzmann function to their activation curves [$V_{0.5}$ = −28.1 ± 1.7 mV (SD), Fig. 3*B*]. Given the noise of the fluorescence–voltage relationships of the individual AZs we approximated the data by a fit function (*SI Methods*) and then analyzed the derived fractional activation curves by fitting a Boltzmann function. The mean $V_{0.5}$ of synaptic Ca^{2+} influx at 210 AZs of these IHCs (−27.4 mV) was very similar to that of the mean whole-cell Ca^{2+} influx. However, fractional activation varied substantially among the AZs (Fig. 3*C*). Accordingly, the $V_{0.5}$ of Ca^{2+} influx showed a wide distribution for the entire AZ population, ranging from −38.4 mV to −18.1 mV (SD: 4.7 mV, Fig. 3 *C* and *D*) and within the individual IHCs [mean: −27.3 ± 3.2 mV (SD), Fig. S1*G*]. The voltage sensitivity of Ca^{2+} influx reported by the slope factor k was similar for whole-cell and synaptic Ca^{2+} influx (7.2 ± 0.4 mV vs. 8.2 ± 1.5 mV, Fig. 3 *B* and *E*). The scatter plot of slope factor

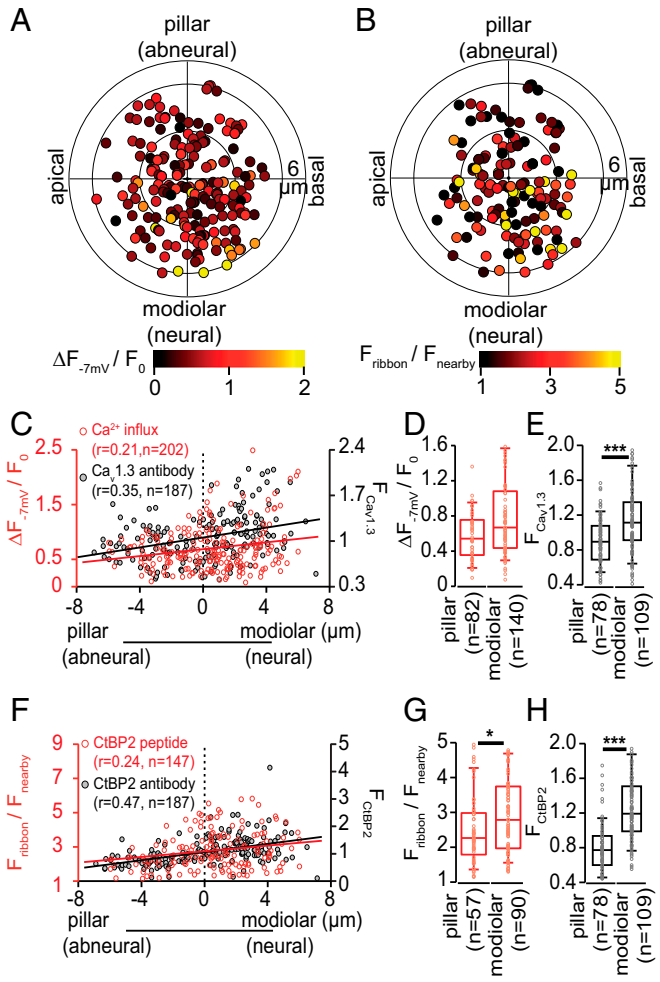

Fig. 2. Maximal synaptic Ca^{2+} influx varies with AZ position in IHCs: modiolar–pillar gradient. (*A*) The polar chart displays intensity of maximal AZ Ca^{2+} influx ($\Delta F_{-7\ mV}/F_0$) as a function of AZ position in live-imaging experiments. Modiolar and pillar refer to facing toward or away from the ganglion in the modiolus; apical and basal refer to the tonotopic axis of the organ of Corti. The radius of the inner circle is 3 µm. Data were pooled from 21 IHCs. (*B*) The polar chart displays locations and intensity of AZ TAMRA-peptide fluorescence intensity in live-imaging experiments. Data were pooled from 14 IHCs. (*C*) Maximal AZ Ca^{2+} influx (red, 202 AZs of 21 cells) and integrated AZ $Ca_V1.3$ immunofluorescence (black, 187 AZs of 12 cells) as a function of position along the modiolar–pillar axis. Solid lines represent linear regressions and r indicates the Pearson's correlation coefficient. (*D*) The box plot (10, 25, 50, 75, and 90% percentiles) shows the statistics of maximal AZ Ca^{2+} influx for the modiolar (140 AZs) and pillar (82 Azs) halves of the same IHCs as in *A*. No significant difference was reported by Wilcoxon rank sum test ($P = 0.33$). (*E*) The box plot shows the statistics (as in *D*) of $Ca_V1.3$ immunofluorescence intensity for AZs of 12 cells, which was stronger on the modiolar (109 AZs) than on the pillar side (78 AZs, $P < 0.001$). (*F*) Spatial gradient of AZ TAMRA-peptide fluorescence in live-imaging (red, 14 IHCs) and CtBP2/RIBEYE immunofluorescence (black circle, same AZs as in *E*) along the modiolar–pillar axis. (*G* and *H*) The box plot shows the statistics (as in *D*) of the TAMRA-peptide fluorescence intensity (*G*) and CtBP2/RIBEYE immunofluorescence intensity (*H*). Both measures indicate greater CtBP2/RIBEYE abundance on the modiolar side than on the pillar side: *G*, $P < 0.05$ and *H*, $P < 0.001$.

and $V_{0.5}$ (Fig. 3*F*) also presents the maximal Ca^{2+} influx (color scale) for a total of 210 AZs: The synapses with the strongest maximal Ca^{2+} influx showed intermediate $V_{0.5}$. We found a tendency for synapses with more hyperpolarized $V_{0.5}$ to have greater voltage sensitivity (i.e., smaller k; $r = 0.47$).

We found that, on average, Ca^{2+} influx at pillar AZs had slightly more hyperpolarized $V_{0.5}$ than that of the modiolar ones (Fig. 4 *A* and *B*, ~1.4 mV, $P < 0.001$, Wilcoxon rank sum test), whereas there was no significant difference in voltage sensitivity between pillar and modiolar synapses (Fig. 4 *C* and *D*, $P > 0.05$, Wilcoxon rank sum test). We did not detect gradients along the tonotopic and central axes of the IHCs for either $V_{0.5}$ or k (Fig. S4 *B* and *C*). In summary, our data indicate major differences in presynaptic Ca^{2+} signaling for a given receptor potential. This may translate into differences in transmitter release and postsynaptic spiking. The more negative operating point of pillar AZs might account for the high spontaneous rates and low sound thresholds of SGNs emanating from pillar synapses reported for the cat. How the pillar–modiolar gradient of the voltage dependence of Ca^{2+} influx

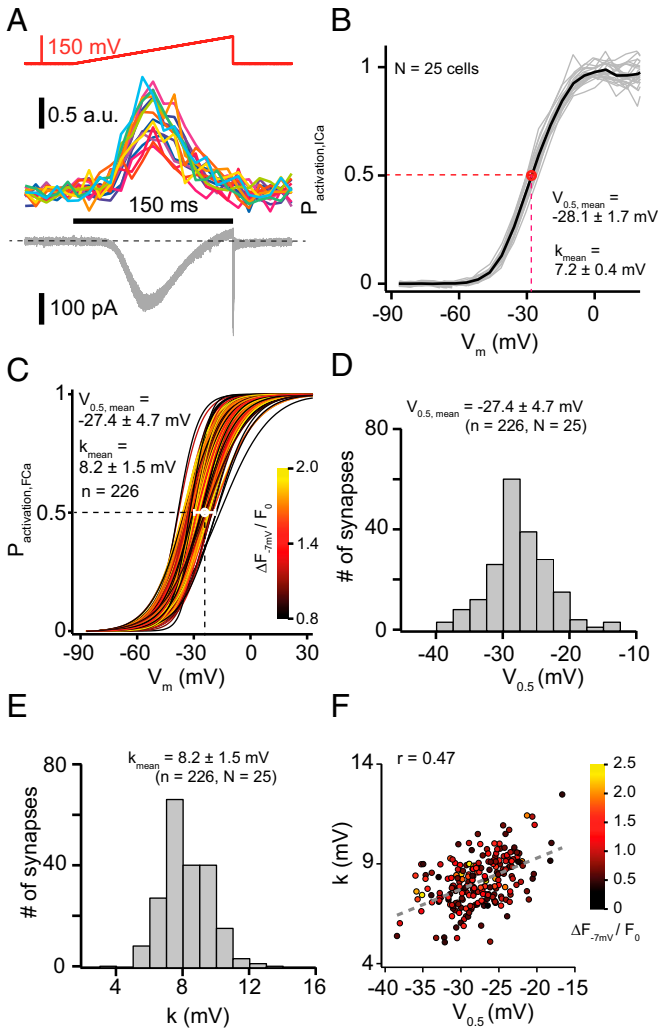

Fig. 3. Heterogeneity of voltage-dependent activation of AZ Ca^{2+} influx in IHCs. (*A*) Representative experiment analyzing voltage-dependent activation of AZ Ca^{2+} influx. Ramp depolarizations were used (*Upper*: from –87 mV to 63 mV in 150 ms, that is, 1 mV/ms), which elicited Ca^{2+} influx at the AZs (*Middle*) and whole-cell Ca^{2+} currents (*Lower*) within an individual cell. (*B*) Fractional activation of the whole-cell Ca^{2+} current: data from 25 IHCs (gray) and average (black). The red circle and error bars indicate the mean and SD of $V_{0.5}$ of these 25 IHCs. (*C*) Fractional activation of 210 AZs, which are coded by colors according to their $\Delta F_{-7\ mV}/F_0$. The white circle and bars represent the mean and SD of the $V_{0.5}$ of Ca^{2+} influx at these AZs. (*D* and *E*) Histograms of $V_{0.5}$ (*D*) or slope factor k (*E*) of all AZs along with mean and SD. (*F*) Relation of $V_{0.5}$ and k of the 210 AZs with color indicating their maximal Ca^{2+} influx. The gray dashed line represents a line fit to the k vs. $V_{0.5}$ relationship with $r = 0.47$.

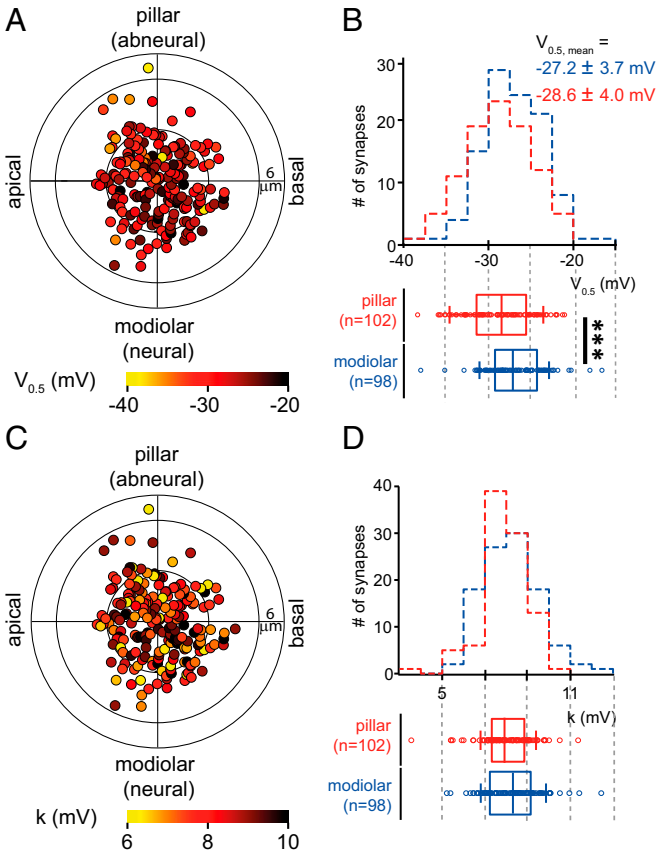

Fig. 4. Spatial gradients of voltage-dependent activation of AZ Ca^{2+} influx. (*A* and *C*) Polar charts display $V_{0.5}$ (*A*) and k (*C*) of 210 AZs of 25 IHCs as a function of AZs location within IHCs (as in Fig. 2*A*). (*B* and *D*) (*Upper*) Histograms of $V_{0.5}$ (*B*) or k (*D*) of AZs on the modiolar side (blue) and pillar side (red). (*Lower*) The box plots of $V_{0.5}$ or k for pillar and modiolar AZs. $V_{0.5}$ was more hyperpolarized for pillar AZs than for modiolar AZs ($P < 0.001$, Wilcoxon rank sum test). Modiolar and pillar AZs did not show statistically significant differences in k.

may be reconciled with the opposing modiolar–pillar gradient of maximal Ca^{2+} influx is discussed below.

Probing Molecular Candidate Mechanisms for Regulation of Synaptic Ca^{2+} Influx. How does the IHC, a compact presynaptic cell, establish heterogeneity of Ca^{2+} influx among its AZs? Here, we considered two classes of candidate mechanisms: (*i*) differences in the subunit composition of the Ca^{2+}-channel complex and (*ii*) different interaction partners. The pore-forming $Ca_V1.3\alpha$ and the auxiliary $Ca_V\beta_2$ are the dominating subunits of IHC Ca^{2+}-channel complexes, but other subunits contribute (27, 28, 32, 33). Differences in the biophysical properties of $Ca_V1.3$ Ca^{2+} channels among IHC AZs might arise from the preferential abundance of specific auxiliary subunits (32, 33) or splice variants of the pore-forming α subunit (34, 35).

Indeed, analysis of splice variants with short C terminus or long C terminus, both expressed by IHCs (36), in HEK293 cells revealed more hyperpolarized activation and higher open probability for short splice variants of the channel (34, 35). Here, we studied synaptic Ca^{2+} influx in IHCs of knock-in mice expressing the pore-forming $Ca_V1.3\alpha$ with an HA-tag in exon 49 (36). The HA-tag disrupts the C-terminal automodulatory domain in the long $Ca_V1.3\alpha$ splice variant. This preserves potential C-terminal protein interaction domains but when expressed in HEK293 cells functionally converts the gating of "long" splice variants to that of "short" ones. Therefore, we expected to find more hyperpolarized activation of synaptic Ca^{2+} influx. However, the mean $V_{0.5}$ (*t* test) and its variance (Levene's test) were unchanged (Fig. 5 *A*–*C*), whereas the maximal AZ Ca^{2+} influx (Fig. 5 *D* and *E*, $P < 0.005$, Wilcoxon rank sum test) and whole-cell Ca^{2+} current (Fig. 5*F*)

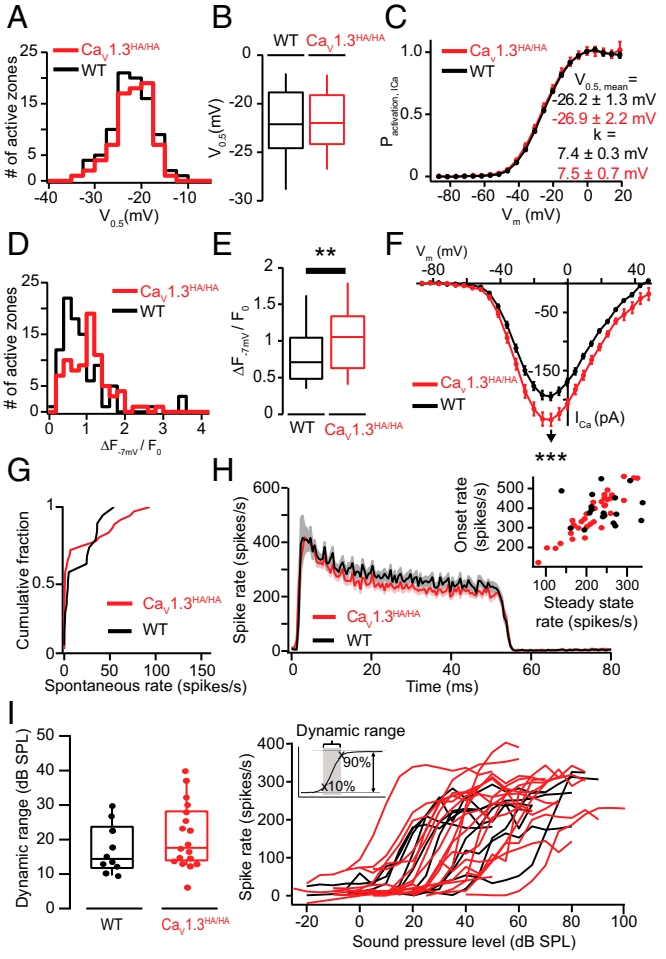

Fig. 5. Disrupting the C-terminal regulatory domain of $Ca_V1.3$ does enhance maximal synaptic Ca^{2+} influx but does not alter $V_{0.5}$ heterogeneity and sound encoding. (*A*) Distributions of $V_{0.5}$ of the AZ Ca^{2+} influx in $Ca_V1.3^{HA/HA}$ (red, 76 AZs of 10 IHCs) and WT (black, 89 AZs of 10 IHCs) mice. Experiments were performed as in Fig. 3. (*B*) Box-whisker charts of $V_{0.5}$ of the AZ Ca^{2+} influx: nonsignificant differences for $Ca_V1.3^{HA/HA}$. (*C*) Comparable fractional activation of Ca^{2+} current as a function of voltage for IHCs of both genotypes. Neither $V_{0.5}$ nor k has significant differences observed between the two different mouse strains. Experiments and analysis were conducted as described in *SI Methods*. (*D*) Distributions of maximal AZ Ca^{2+} influx in $Ca_V1.3^{HA/HA}$ (red, 79 AZs of 10 IHCs) and control (black, 94 AZs of 10 IHCs) mice. Experiments were performed as in Fig. 1*B*. (*E*) Box-whisker charts of maximal AZ Ca^{2+} influx in $Ca_V1.3^{HA/HA}$ IHCs, which was significantly stronger than that of WT IHCs ($P < 0.01$, Wilcoxon rank sum test). (*F*) Current–voltage relationship of the whole-cell Ca^{2+} current of IHC in WT (black) or $Ca_V1.3^{HA/HA}$ (red). The $Ca_V1.3^{HA/HA}$ IHC has larger maximal Ca^{2+} current than the WT cells ($P < 0.001$, $I_{Ca,-7\ mV,WT} = -194.6 \pm 6.6$ pA, $I_{Ca,-7\ mV,HA} = -234.6 \pm 10.6$ pA). The errors in this panel are SEM. (*G*) Histogram showing the spontaneous rate distribution of $Ca_V1.3^{HA/HA}$ and WT SGNs. (*H*) Average poststimulus time histogram of SGN responses to 50-ms suprathreshold tone bursts at the characteristic frequency. Both the onset (average firing rate in a 1-ms window after median first spike latency) and steady-state rate (average firing rate over the last 5-ms window of 50-ms tone bursts) did not differ significantly between $Ca_V1.3^{HA/HA}$ and WT SGNs. (*I*) Rate-level functions (*Right*) and dynamic range (*Left*) for $Ca_V1.3^{HA/HA}$ and WT SGNs. Dynamic range is defined as the range of sound pressure levels in which the rate-level function showed a rate increase between 10% and 90% of the difference between spontaneous and maximum rate. No statistically significant difference between the dynamic ranges was observed between $Ca_V1.3^{HA/HA}$ and WT SGNs (19 for $Ca_V1.3^{HA/HA}$ vs. 10 for WT SGNs, not significant by Wilcoxon rank sum test).

were larger. Next, we studied sound encoding at the single SGN level in $Ca_V1.3^{HA/HA}$ mice and found a normal distribution of spontaneous firing rates (Fig. 5*G*), normal sound-evoked firing rates (Fig. 5*H*), and normal sound-pressure dependence of firing (Fig. 5*I*). The observed lack of effect of the C-terminal $Ca_V1.3\alpha$ manipulation on the voltage dependence of Ca^{2+} current activation may be due to strong regulation of $Ca_V1.3$ in IHCs by interactions with Ca^{2+}-binding proteins (37–39). The increased maximal Ca^{2+} influx, likely resulting from an increased open probability (34), apparently did not change SGN firing behavior.

AZ proteins known to directly or indirectly interact with the Ca^{2+}-channel complex include bassoon (40) and rab-interacting protein (RIM) (41, 42). Both positively regulate the number of Ca^{2+} channels at the IHC AZ (15, 43). Bassoon, moreover, contributes to establishing heterogeneity of maximal Ca^{2+} influx whereas RIM2α does not seem to be required. Another candidate interacting partner is harmonin, which regulates $Ca_V1.3$ Ca^{2+} channels, likely by binding of one of its PDZ domains to the ITTL motif of the extreme $Ca_V1.3$ C terminus (44, 45). Here, we revisited the regulation of IHC AZs by harmonin in deaf-circler mice (*dfcr*) (46), reasoning that site-specific expression of harmonin might contribute to the heterogeneity of maximal Ca^{2+} influx and voltage dependence of activation. *Dfcr* IHCs had weaker RIBEYE-peptide fluorescence regardless of the AZ position (Fig. S5*A*, $P < 0.05$, Wilcoxon rank sum test). AZ Ca^{2+} influx and whole-cell Ca^{2+} current activated at more hyperpolarized potentials (Fig. S5 *B* and *C*, $P < 0.05$, *t* test and Wilcoxon rank sum test, respectively). However, this $V_{0.5}$ shift was observed for both modiolar and pillar *dfcr* AZs (both $P < 0.05$, one-way ANOVA with Tukey's post hoc test), arguing against a substantial contribution of harmonin to presynaptic heterogeneity.

The whole-cell Ca^{2+} influx was enhanced ($P < 0.05$, Wilcoxon rank sum test), but the mean synaptic Ca^{2+} influx was not (Fig. S5*D*), suggesting greater extrasynaptic Ca^{2+} influx in *dfcr* IHCs. To test for IHC immaturity and the greater extrasynaptic Ca^{2+} influx that accompanies it (29), we immunolabeled for $Ca_V1.3$ and large-conductance Ca^{2+}-activated K^+ channels (BK channels, Fig. S5 *E* and *F*). However, $Ca_V1.3$ was confined to synapses, which seemed present at normal numbers, and BK channels clustered at the IHC neck, both indicating IHC maturity. We speculate that the $V_{0.5}$ shift reflects the absence of $Ca_V1.3$ regulation by harmonin or might relate to impaired mechanoelectrical transduction in *dfcr* mice (47).

***Gipc3* Disruption Causes a Hyperpolarized Shift in Ca^{2+} Channel Activation and Enhances Spontaneous SGN Firing.** Another PDZ protein and candidate regulator of Ca^{2+} channels and AZ heterogeneity is Gipc3 (GAIP interacting protein, C terminus 3). Defects of the human *GIPC3* gene cause human deafness (48, 49) and *Gipc3* disruption in mice lead to audiogenic seizures and progressive hearing loss (48). GIPC proteins share a central PDZ domain flanked by GIPC homologous domains. Gipc1 has broad roles in intracellular protein trafficking and in hair cells is required for development of stereocilia bundles and planar cell polarity (50–52). We studied Black Swiss (BLSW, hereafter *Gipc3* mutant) mice that carry a missense mutation in the *Gipc3* gene (c.343G > A), which replaces a highly conserved glycine with an arginine at position 115 (Gly115Arg) located within the PDZ domain. Early-onset hearing impairment in Gipc3 mutant mice has been attributed to dysfunction of hair cell stereocilia, although its localization within hair cells resembles a cytoplasmic vesicular pattern similar to myosin VI (48). In the brain, glutamate release was shown to depend on interaction between myosin VI and its binding partner Gipc1 (50). In hair cells, a synaptic function for Gipc proteins is yet unknown.

In *Gipc3* mutant IHCs we found an increased whole-cell Ca^{2+} current (Fig. 6 *A* and *D*, $P < 0.05$, Wilcoxon rank sum test) and a more hyperpolarized $V_{0.5}$ of activation [Fig. 6*B*, $P = 0.004$, Wilcoxon rank sum test; *Gipc3* mutant IHCs: $V_{0.5} = -31.2 \pm 1.4$ mV, $n = 19$ compared with C57BL/6J control IHCs (WT): $V_{0.5} = -24.1 \pm 1.8$ mV, $n = 20$]. Moreover, we found Ca^{2+} current inactivation to be reduced in *Gipc3* mutants when comparing Ca^{2+} currents elicited by 500-ms-long depolarizations (I_{res}/I_{peak} 0.59 ± 0.04 for 10 *Gipc3* mutant IHCs vs. 0.41 ± 0.03 for 8 WT IHCs, $P = 0.007$, Wilcoxon rank sum test). We also observed enhanced exocytosis reported as membrane capacitance increments (Fig. 6 *C* and *D*, significant for 50- and 100-ms-long depolarizations), likely as a consequence of the increased Ca^{2+} current. At the AZ level, the distributions of maximal Ca^{2+} influx (Fig. 7*A*) and RIBEYE-peptide fluorescence (Fig. 7*B*) and were comparable to WT, but the $V_{0.5}$ distribution was broader in *Gipc3* mutant IHCs and AZs activated at more hyperpolarized potentials on average (Fig. 6*C*, $P < 0.01$ for variance, Brown–Forsythe test and $P < 0.01$ for mean, Wilcoxon rank sum test). Opposite that in WT, maximal AZ Ca^{2+} influx (Fig. 7*D*) exhibited a pillar–modiolar gradient in

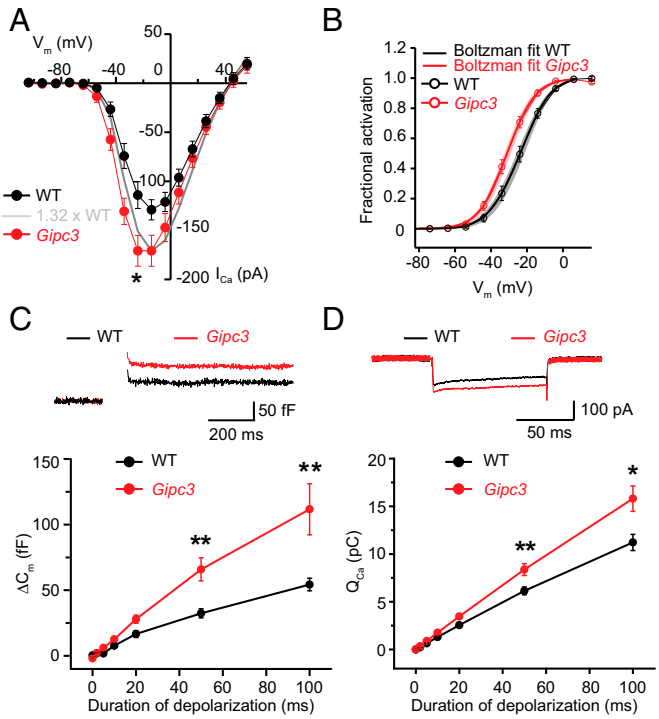

Fig. 6. Disruption of *Gipc3* results in increased amplitude and hyperpolarized shift of activation of IHC Ca^{2+} influx as well as enhanced exocytosis. (*A*) Average steady-state I_{Ca}-V of WT IHCs (black trace, 11 cells) and *Gipc3* IHCs (red trace, 7 cells) acquired with 10-ms-long depolarizations (steady-state Ca^{2+} currents during depolarization): hyperpolarized voltage dependence and increased amplitude ($I_{Ca,-24\ mV,\ WT} = -110.6 \pm 13$ pA, $I_{Ca,-24\ mV,\ Gipc3} = -166.2 \pm 17.3$ pA, <0.05, Wilcoxon rank sum test). Data are shown as mean ± SEM. (*B*) Fractional activation of Ca^{2+} current as a function of voltage for IHCs of WT IHCs (black trace, 19 cells) and *Gipc3* IHCs (red trace, 20 cells). $V_{0.5}$ of *Gipc3* IHCs is significantly different from that of WT IHCs (<0.05, Wilcoxon rank sum test). Data are shown as mean ± SEM. (*C*) (*Upper*) Average capacitance increments (ΔCm) traces of WT IHCs (black trace, 11 cells) and *Gipc3* IHCs (red trace, 8 cells) in response to 100-ms-long step depolarization to −14 mV. (*Lower*) Average ΔCm of p14-16 WT IHCs (black, 11 cells) and *Gipc3* IHCs (red, 8 cells) for depolarizations of different durations. Capacitance increments are significantly increased in *Gipc3* IHCs at depolarizations of 50 ms (WT: 32.4 ± 3.4 fF, *Gipc3*: 65.9 ± 8.7 fF, <0.01, Wilcoxon rank sum test) and 100 ms (WT: 54.3 ± 4.7 fF, *Gipc3*: 111.7 ± 19.4 fF, <0.01, Wilcoxon rank sum test). Data are shown as mean ± SEM. (*D*) (*Upper*) Average Ca^{2+} currents (Q_{Ca}) traces of WT IHCs (black trace, 11 cells) and *Gipc3* IHCs (red trace, 8 cells) in response to 100-ms-long step depolarization to −14 mV. (*Lower*) Average Q_{Ca} corresponding to *C*). Ca^{2+} currents are significantly increased in *Gipc3* IHCs (red) at depolarizations of 50 ms (WT: 6.1 ± 0.4 pC, *Gipc3*: 8.3 ± 0.6 pC, <0.01, Wilcoxon rank sum test) and 100 ms (WT: 11.2 ± 0.8 pC, *Gipc3*: 15.8 ± 1.3 pC, <0.05, Wilcoxon rank sum test). Data are shown as mean ± SEM.

Gipc3 mutants. As a result, the pillar AZs, operating at even more hyperpolarized potentials than in WT, also had stronger maximal Ca^{2+} influx on average (Fig. 7 *D–F*).

To relate these presynaptic observations to SGN firing properties, we performed in vivo recordings of SGN firing in *Gipc3* mutant mice after onset of hearing [postnatal days (p) 14–25]. *Gipc3* mutant mice showed elevated auditory brainstem response (ABR) thresholds at p14 and p21 (Fig. S6 *A* and *B*). Single SGN frequency tuning was broad and thresholds at the characteristic frequency in *Gipc3* mutant mice were elevated on average by 28 dB (2 wk) and 72 dB (3 wk) (Fig. S6 *B–D*). These effects are attributable to impaired mechanoelectrical transduction and cochlear amplification (48). This stereociliary impairment precluded assessment of the influence of the observed hyperpolarized activation of Ca^{2+} channels on sound-response properties. However, in the absence of sound the spontaneous spike rate in SGNs comes from Ca^{2+}-dependent transmitter release from the hair cell at its resting potential (53), allowing us to assess the effects of shifted voltage dependence of AZ Ca^{2+} influx on baseline release. Despite impaired transduction of sound, spontaneous SGN firing

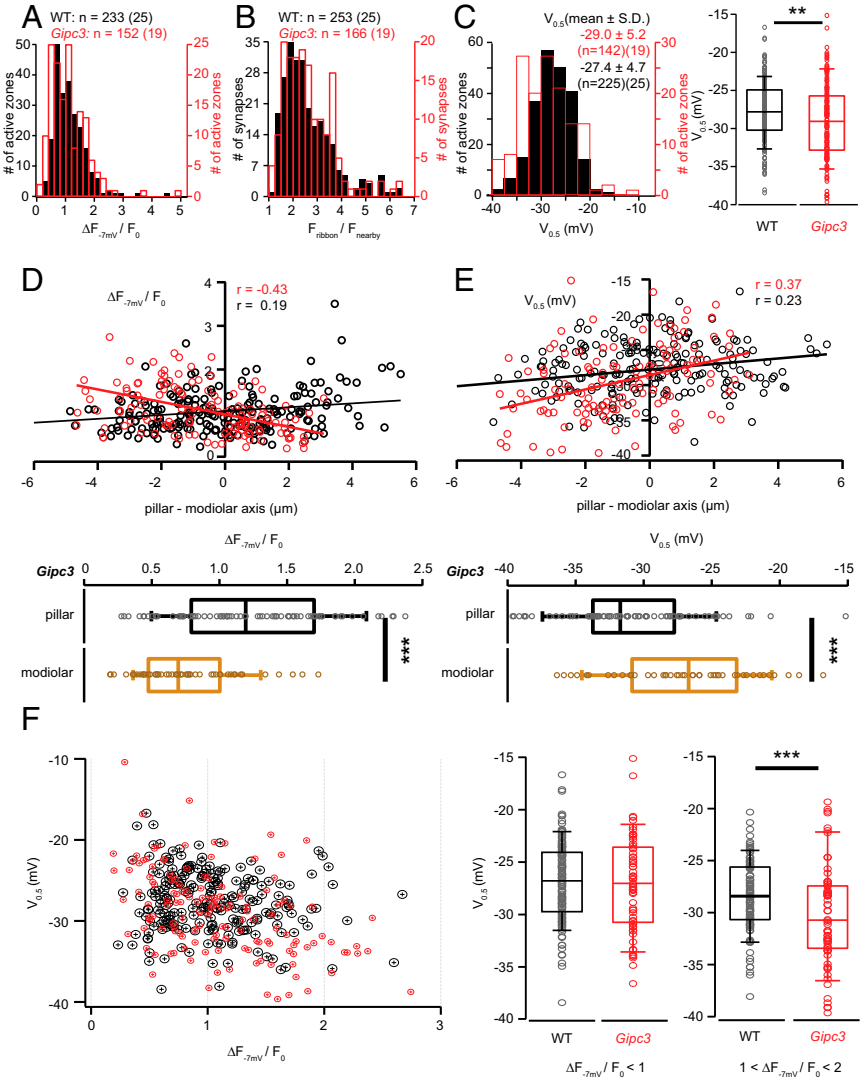

Fig. 7. Disruption of *Gipc3* in mice shifts the activation of Ca^{2+} influx to more hyperpolarized potentials and reverses the modiolar–pillar gradient of maximal Ca^{2+} influx. (*A*) Distribution of maximal AZ Ca^{2+} influx in IHCs of *Gipc3* mutant (red trace, $n = 152$, 19 cells) and WT mice (blue trace, 225 AZs of 25 cells). The experimental protocol is the same as Fig. 1*B*. (*B*) Distribution of the AZ TAMRA-peptide fluorescence in *Gipc3* mutant IHCs (red trace, 166 AZs, 19 IHCs) and WT IHCs (blue trace, 253 AZs of 25 IHCs). (*C*, *Left*) Distribution of $V_{0.5}$ of the voltage-dependent activation of AZ Ca^{2+} influx in *Gipc3* mutant IHCs (red trace, 142 AZs of 19 IHCs) and WT IHCs (blue trace, $n = 225$, 25 cells). The experimental protocol is the same as Fig. 3*A*. (*C*, *Right*) Box plot of $V_{0.5}$ of voltage-dependent activation of AZ Ca^{2+} influx in *Gipc3* mutant IHCs: $V_{0.5}$ was significantly more hyperpolarized in *Gipc3* mutant IHCs ($P < 0.01$, Wilcoxon rank sum test). (*D*, *Upper*) Opposing gradients of maximal AZ Ca^{2+} influx in *Gipc3* (red circle, 128 AZs of 19 IHCs) and WT (blue circle, 226 AZs of 25 IHCs) along the modiolar–pillar axis. Solid lines are their fitting lines, r indicates their correlation coefficients. (*D*, *Lower*) The box plots summarize the distributions of maximal Ca^{2+} influx of pillar and modiolar AZs for *Gipc3* mutant IHCs. The maximal AZ Ca^{2+} influx of pillar AZs was significantly stronger than that of pillar AZs ($P < 0.001$, Wilcoxon rank sum test). (*E*) (*Upper*) Spatial distribution of the $V_{0.5}$ in *Gipc3* mutant IHCs (red circle, 119 AZs of 19 IHCs) and WT IHCs (blue, 194 AZs, 21 IHCs) along the modiolar–pillar axis. Solid lines are line fits to the data. (*E*, *Lower*) Box plots summarize the $V_{0.5}$ distributions of pillar and modiolar AZs in *Gipc3* mutant IHCs. The $V_{0.5}$ of pillar AZs was significantly more hyperpolarized than that of modiolar AZs ($P < 0.001$, Wilcoxon rank sum test). (*F*, *Left*) The relationship of maximal AZ Ca^{2+} influx and $V_{0.5}$ (red: *Gipc3*, blue: WT). (*F*, *Right*) Box-whisker charts summarize the distributions of $V_{0.5}$ in subgroups of their $\Delta F_{-7\ mV}/F_0$: smaller than 1 (*Left*) and between 1 and 2 (*Right*). $V_{0.5}$ of AZs from *Gipc3* mutant IHCs were more hyperpolarized (−30.2 ± 4.9 mV) than those of WT IHCs (−28.4 ± 3.5 mV, $P < 0.001$, Wilcoxon rank sum test) for the subgroup of AZs with $\Delta F_{-7\ mV}/F_0$ is between 1 and 2, whereas it was statistically indistinguishable for the AZ subgroup with smaller maximal Ca^{2+} influx.

rates were elevated in *Gipc3* mutant mice ($P < 0.05$, one-sided Kolmogorov–Smirnov test). In contrast to WT animals, where about 50% of SGNs had a spontaneous rate below 20 Hz, only 16% of SGNs in *Gipc3* mutant mice exhibited spontaneous rates below 20 Hz (Fig. 8*A*). Some low-spontaneous-rate SGNs, which generally have higher thresholds, may not have been activated by the highest-intensity search stimuli (100-dB sound pressure level). Regardless, we found a greater abundance of SGNs with high spontaneous firing rates (28% with rates >50 Hz vs. only 12% in WT).

Despite elevated thresholds in *Gipc3* mutant mice that most likely resulted from impaired mechanotransduction and cochlear amplification, firing rates at sound onset were elevated when probed at 30 dB above threshold with tone bursts at the characteristic frequency in 2- to 3-wk-old mice. SGNs had onset rates of 451.4 ± 27.0 Hz for *Gipc3* mutant ($n = 25$) vs. 347.1 ± 26.1 Hz for WT ($n = 24$, $P < 0.05$, Wilcoxon rank sum test). In contrast, the adapted firing rates were indistinguishable from WT (Fig. 8*B*). Consistent with the defect of cochlear amplification, rate vs. level functions had steeper slopes and significantly narrower dynamic ranges (Fig. 8*C*). Recovery from adaptation, most likely reflecting presynaptic replenishment of the readily releasable pool, proceeded at normal pace in *Gipc3* mutant mice (Fig. S6*F*).

In principle, the increased spontaneous discharge rates of SGNs in *Gipc3* mutant mice could have resulted from a more depolarized IHC resting membrane potential, potentially due to reduced basolateral K^+ conductances (48). However, IHC resting membrane potentials were unaltered (Fig. S7*A*), BK channels clustered at the neck as in WT (Fig. S7*B*), and BK currents were normally sized (Fig. S7*C*) in *Gipc3* mutant IHCs at p14–16, indicating normal IHC maturation (54). This notion was further corroborated by the normal number of ribbon synapses (Fig. S7*D*). In conclusion, disruption of *Gipc3* produced a shift of Ca^{2+}-current activation toward hyperpolarized potentials, reversed the modiolar–pillar gradient of maximal Ca^{2+} influx at IHC AZs, and increased spontaneous firing rates in SGNs.

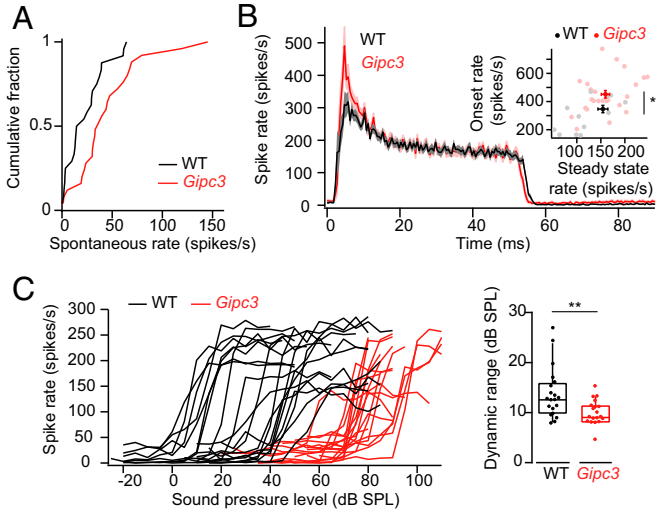

Fig. 8. *Gipc3* disruption enhances spontaneous SGN firing. (*A*) Cumulative histogram of spontaneous rate distribution: no major overlap of the data. WT (C57BL/6) data were taken from ref. 19. The spontaneous rate of *Gipc3* SGNs showed a shift of mean about 21.5 Hz in comparison with that of WT SGNs. The null hypothesis that the spontaneous discharge rates *Gipc3* and WT SGNs came from populations with the same distribution was rejected, and the alternative hypothesis that the cumulative distribution function of WT was larger than that of *Gipc3* SGNs was favored ($P < 0.05$, one-sided Kolmogorov–Smirnov test). (*B*) Peristimulus time histogram of 3-wk-old *Gipc3* and WT SGNs to 50-ms suprathreshold tone bursts at the characteristic frequency. The onset firing rates of *Gipc3* were elevated (451.4 ± 27.0 Hz for *Gipc3* mutant, 25 SGNs vs. 347.1 ± 26.1 Hz for WT, 24 SGNs, $P < 0.05$). The steady-state firing rates did not differ significantly (159.5 ± 8.6 Hz for *Gipc3* mutant, 25 SGNs vs. 154.3 ± 10.4 Hz for WT, 24 SGNs, not significant by Wilcoxon rank sum test). (*C*) Rate-intensity functions (*Left*) and dynamic range (*Right*) of sound encoding in *Gipc3* and WT SGNs. *Gipc3* SGNs had a narrower dynamic range than WT SGNs (9.9 ± 0.6 dB for *Gipc3* p14–25, 19 SGNs vs. 13.7 ± 1.1 dB for WT p14–21, 20 SGNs, $P < 0.01$, Wilcoxon rank sum test).

Discussion

The ear encodes changes in sound pressure over six orders of magnitude using SGNs that change their firing rates over different fractions of the audible range, but the mechanisms underlying such dynamic range fractionation are unknown. Therefore, we used fluorescence imaging to characterize heterogeneity among AZs in cochlear IHCs as a candidate mechanism. Our study indicates that IHCs decompose information on sound intensity into different outputs by varying the Ca^{2+} influx among their AZs. Two key determinants of presynaptic Ca^{2+} influx, the voltage dependence and the number of Ca^{2+} channels, differed greatly among the AZs within IHCs and exhibited shallow opposing spatial gradients along the pillar–modiolar IHC axis. AZs of the pillar face, on average, were smaller but activated at more hyperpolarized potentials and, hence, are likely presynaptic to high-spontaneous-rate, low-threshold SGNs. The number of $Ca_V1.3$ Ca^{2+} channels and maximal synaptic Ca^{2+} influx, on average, were greater for modiolar AZs, which also were larger in size. We propose that these AZs, given their more depolarized operation range, are recruited by stronger sounds and likely drive low-spontaneous-rate, high-threshold SGNs. Disruption of *Gipc3* reversed the normal modiolar–pillar gradient of maximal AZ Ca^{2+} influx, shifted Ca^{2+} channel activation to more hyperpolarized potentials, and increased the fraction of SGNs with high-spontaneous firing rate.

Dynamic Range Fractionation Through Heterogeneity of Synaptic Voltage Dependence. Each presynaptic AZ in a given IHC is controlled by a common potential and provides the sole excitatory input to "its" postsynaptic SGN. How the operating range of Ca^{2+} influx at an AZ matches the IHC resting and receptor potential critically determines its transmitter release and hence the spontaneous and sound-evoked firing of the postsynaptic SGN. Because technically challenging in vivo tight-seal patch-clamp recordings from IHCs have not yet been achieved there is uncertainty about the resting (in quiescence) and the receptor (during sound stimulation) potential. Pioneering recordings with sharp electrodes from guinea pig IHCs indicated a resting potential of –40 mV and maximal receptor potentials between ~10 and 30 mV (1), and a patch-clamp study trying to emulate physiological ionic conditions in the explanted gerbil organ of Corti estimated a resting potential of –55 mV (55). Regardless of the precise resting potential it is evident that Ca^{2+} influx is partially active at least at a subset of IHC AZs (Fig. 3) and the relatively depolarized IHC resting potential is expected to facilitate Ca^{2+} influx and transmitter release (56, 57). Moreover, the range covered by Ca^{2+} activation at the various AZs ($V_{0.5}$ spanning from –38 mV to –18 mV) matches the reported range of IHC receptor potentials very well (Fig. 3). The SGNs with identical frequency tuning but different sound-response properties presumably receive input from the same IHC and collectively convey acoustic information across the entire audible range of sound pressures to the brain. Candidate mechanisms underlying the diversity of SGN response properties include presynaptic (7, 11, 12), postsynaptic (13), and efferent (17, 18) mechanisms. Here, we asked how IHCs might fractionate the auditory signal for different parallel outputs through heterogeneous Ca^{2+} influx among AZs. Fast 3D live imaging enabled us to analyze functional and morphological properties of most, if not all, AZs as a function of position within an individual IHC. In parallel, we performed semiquantitative confocal microscopy of immunolabeled IHC synapses. AZs differed considerably in size, number, and voltage dependence of Ca^{2+} channels whereby differences

among AZs within individual IHCs explained most of the variance of the entire AZ population. The estimates for Ca^{2+}-channel number were positively correlated with our proxy of AZ size in both live-imaging and immunohistochemistry experiments, even at the level of the single IHC.

Modiolar AZs were larger, had more Ca^{2+} channels, and tended to show stronger maximal Ca^{2+} influx. The hypothesis that these AZs drive SGNs with lower spontaneous firing rate and higher sound threshold, at first sight, seems counterintuitive because a greater number of Ca^{2+} channels is expected to elicit more spontaneous and evoked release. However, we found that modiolar AZs, on average, required more depolarization for their activation (Fig. 4), consistent with the idea that modiolar synapses drive high-threshold SGNs (2, 7, 8). Modiolar AZs that hold more Ca^{2+} channels may support higher maximal rates of transmitter release, which could explain the higher susceptibility of low-spontaneous-rate, high-threshold SGNs to excitotoxic insult during acoustic overexposure (58). The operation of pillar AZ at relatively hyperpolarized potentials may contribute to high-spontaneous firing rates and responses to soft sounds found for SGNs innervating the pillar side (2, 7). Based on the spatial distribution of the voltage dependence of presynaptic Ca^{2+} influx found here for mice, and the spatial distribution of postsynaptic spontaneous rates in cats, we hypothesize that the voltage dependence of presynaptic Ca^{2+} influx is a major determinant of spontaneous and sound-driven SGN firing. This hypothesis is supported by the more hyperpolarized $V_{0.5}$ of AZ Ca^{2+} influx in IHCs (Fig. 7) and the increase in SGN spontaneous firing rates in *Gipc3* mutant mice (Fig. 8), but not in in $Ca_V1.3^{HA/HA}$ mice, for which, too, we found more AZ Ca^{2+} influx but no change in voltage dependence. However, we note that different from classic experiments in mature cats (2, 7) the present data were obtained from mice and we cannot rule out some immaturity of the afferent synaptic connectivity because we recorded soon after the onset of hearing. Moreover, the variability of voltage dependence of presynaptic Ca^{2+} influx was high in both the modiolar and pillar halves, whereby the differences between $V_{0.5}$ among modiolar or pillar synapses could exceed that between the average pillar and modiolar synapse. In addition, the spatial segregation of functionally distinct classes of type SGNs at the level of IHC innervation in mice might deviate from that described for cats. Future experiments simultaneously addressing presynaptic properties and postsynaptic firing will be required to further test our hypothesis.

Regulation of the Number and Voltage Dependence of Ca^{2+} Channels at IHC AZs. Which mechanisms determine the number and voltage dependence of Ca^{2+} channels at an AZ? The number of Ca^{2+} channels at the presynaptic AZ is governed by the expression of the specific Ca^{2+}-channel subunits and splice variants (33, 36, 59) as well as by that of scaffold proteins that tether Ca^{2+} channels to the AZ (15, 42, 43, 60, 61) and/or regulate their turnover (44) by direct or indirect interaction with the channels. Moreover, subunit composition as well as splice variants and interacting proteins also modulate functional properties of the specific Ca^{2+} channel (62). The Ca^{2+}-channel complex at IHC AZs is likely composed of splice variants of the pore-forming subunit $Ca_V1.3\alpha$ containing exons 43S or 43L (36), of the $Ca_V\beta2$ (33), and less likely of other $Ca_V\beta$ subunits (32), and of a yet-to-be-identified $Ca_V\alpha2\delta$ subunit. $Ca_V\beta2$, the synaptic ribbon, and the presynaptic scaffolds bassoon and RIM2α and β were previously shown to promote the abundance of $Ca_V1.3$ at IHC AZs (15, 33, 43), whereas harmonin seems to reduce the number of synaptic $Ca_V1.3$ (44). Work in zebrafish hair cells has revealed an intriguing molecular interplay between RIBEYE and $Ca_V1.3$ channels, whereby RIBEYE overexpression promotes the formation of $Ca_V1.3$-positive AZ-like specializations and synaptic Ca^{2+} influx negatively regulates RIBEYE abundance at the AZ (63, 64). The present study corroborates the notion that the Ca^{2+}-channel number is proportional to ribbon size in cochlear hair cells (11, 30). We speculate that release rate for a given open probability scales linearly with the number of Ca^{2+} channels, assuming nanodomain coupling (29, 65, 66), regardless of the AZ size. Future simultaneous measurements of AZ Ca^{2+} influx and exocytosis or SGN firing will be required to analyze the consequences of presynaptic heterogeneity for transmitter release at IHC AZs.

How do IHCs form opposing gradients of AZ size, $Ca_V1.3$ abundance, and voltage dependence of activation? The modiolar–pillar gradient of AZ size was lost upon lesion of the lateral olivocochlear efferents (18), and it is tempting to speculate that they provide an instructive influence on the postsynaptic SGN terminal and/or the IHC AZ. Here, we found that the intracellular gradient of maximal Ca^{2+} influx was altered in *Gipc3* mutant mice. In addition, *Gipc3* disruption increased Ca^{2+} influx and caused a hyperpolarizing shift in its activation. These presynaptic changes likely underlie the enhanced spontaneous and sound-onset firing in *Gipc3* mutant mice, although alternative explanations exist. How the Gipc3 protein might be involved directly or indirectly for establishing a modiolar–pillar gradient remains to be elucidated. Considering analogy to Gipc1 (50, 52), it is tempting to speculate that Gipc3 serves to adapt components of the Ca^{2+}-channel complex to motor proteins and thereby assists their trafficking to AZs with a preference for the modiolar face. Signals instructing polarized trafficking might originate from lateral olivocochlear fibers, SGNs themselves, and/or the planar cell polarity that sets the orientation of the apical hair bundle (67, 68) and involves Gipc1 signaling (50). Future work should address the mechanism by which Gipc3 operates to traffic and/or regulate Ca^{2+} channels.

Methods

Research followed national animal care guidelines and was approved by the University of Göttingen board for animal welfare and the animal welfare office of the state of Lower Saxony. For details of patch-clamp and confocal Ca^{2+} imaging, immunohistochemistry and confocal imaging, extracellular recordings from auditory nerve fibers, and data analysis see *SI Methods*.

ACKNOWLEDGMENTS. We thank S. Gerke, C. Senger-Freitag, and N. Herrmann for expert technical assistance and Dr. Konrad Noben-Trauth for providing us with Black Swiss mice (*Gipc3* mutant). This work was supported by a scholarship from the German Academic Exchange Service (T.-L.O.), by a fellowship from the Alexander von Humboldt Foundation (M.A.R.), funding from MED-EL, an international project grant from Action on Hearing Loss, and the Department of Otolaryngology at Washington University in St. Louis. This work was also supported by the German Federal Ministry of Education and Research through Bernstein Focus for Neurotechnology Grant 01GQ0810 (to T.M.) and the German Research Foundation through the Collaborative Research Center 889 [Projects A2 (to T.M.) and A6 (to N.S.)], Center for Nanoscale Microscopy and Molecular Physiology of the Brain Grants ECX 101 and FZT 103 (to T.M.), the Leibniz Program (T.M.), and Austrian Science Fund Grant FWF F44020 (to Jörg Striessnig).

1. Russell IJ, Sellick PM (1983) Low-frequency characteristics of intracellularly recorded receptor potentials in guinea-pig cochlear hair cells. *J Physiol* 338(1): 179–206.
2. Liberman MC (1978) Auditory-nerve response from cats raised in a low-noise chamber. *J Acoust Soc Am* 63(2):442–455.
3. Sachs MB, Abbas PJ (1974) Rate versus level functions for auditory-nerve fibers in cats: Tone-burst stimuli. *J Acoust Soc Am* 56(6):1835–1847.
4. Taberner AM, Liberman MC (2005) Response properties of single auditory nerve fibers in the mouse. *J Neurophysiol* 93(1):557–569.
5. Winter IM, Robertson D, Yates GK (1990) Diversity of characteristic frequency rate-intensity functions in guinea pig auditory nerve fibres. *Hear Res* 45(3):191–202.
6. Zagaeski M, Cody AR, Russell IJ, Mountain DC (1994) Transfer characteristic of the inner hair cell synapse: steady-state analysis. *J Acoust Soc Am* 95(6):3430–3434.
7. Merchan-Perez A, Liberman MC (1996) Ultrastructural differences among afferent synapses on cochlear hair cells: Correlations with spontaneous discharge rate. *J Comp Neurol* 371(2):208–221.
8. Liberman MC (1982) Single-neuron labeling in the cat auditory nerve. *Science* 216(4551):1239–1241.

9. Kiang NY, Pfeiffer RR, Warr WB, Backus AS (1965) Stimulus coding in the cochlear nucleus. *Trans Am Otol Soc* 53:35–58.
10. Wen B, Wang GI, Dean I, Delgutte B (2009) Dynamic range adaptation to sound level statistics in the auditory nerve. *J Neurosci* 29(44):13797–13808.
11. Frank T, Khimich D, Neef A, Moser T (2009) Mechanisms contributing to synaptic Ca^{2+} signals and their heterogeneity in hair cells. *Proc Natl Acad Sci USA* 106(11): 4483–4488.
12. Grant L, Yi E, Glowatzki E (2010) Two modes of release shape the postsynaptic response at the inner hair cell ribbon synapse. *J Neurosci* 30(12):4210–4220.
13. Liberman LD, Wang H, Liberman MC (2011) Opposing gradients of ribbon size and AMPA receptor expression underlie sensitivity differences among cochlear-nerve/hair-cell synapses. *J Neurosci* 31(3):801–808.
14. Kantardzhieva A, Liberman MC, Sewell WF (2013) Quantitative analysis of ribbons, vesicles, and cisterns at the cat inner hair cell synapse: Correlations with spontaneous rate. *J Comp Neurol* 521(14):3260–3271.
15. Frank T, et al. (2010) Bassoon and the synaptic ribbon organize Ca^{2+} channels and vesicles to add release sites and promote refilling. *Neuron* 68(4):724–738.
16. Meyer AC, et al. (2009) Tuning of synapse number, structure and function in the cochlea. *Nat Neurosci* 12(4):444–453.
17. Ruel J, et al. (2001) Dopamine inhibition of auditory nerve activity in the adult mammalian cochlea. *Eur J Neurosci* 14(6):977–986.
18. Yin Y, Liberman LD, Maison SF, Liberman MC (2014) Olivocochlear innervation maintains the normal modiolar-pillar and habenular-cuticular gradients in cochlear synaptic morphology. *J Assoc Res Otolaryngol* 15(4):571–583.
19. Wong AB, et al. (2013) Concurrent maturation of inner hair cell synaptic Ca^{2+} influx and auditory nerve spontaneous activity around hearing onset in mice. *J Neurosci* 33(26):10661–10666.
20. Ariel P, Hoppa MB, Ryan TA (2013) Intrinsic variability in Pv, RRP size, Ca^{2+} channel repertoire, and presynaptic potentiation in individual synaptic boutons. *Front Synaptic Neurosci* 4:9.
21. Holderith N, et al. (2012) Release probability of hippocampal glutamatergic terminals scales with the size of the active zone. *Nat Neurosci* 15(7):988–997.
22. Sheng J, et al. (2012) Calcium-channel number critically influences synaptic strength and plasticity at the active zone. *Nat Neurosci* 15(7):998–1006.
23. Roberts WM, Jacobs RA, Hudspeth AJ (1990) Colocalization of ion channels involved in frequency selectivity and synaptic transmission at presynaptic active zones of hair cells. *J Neurosci* 10(11):3664–3684.
24. Issa NP, Hudspeth AJ (1996) The entry and clearance of Ca^{2+} at individual presynaptic active zones of hair cells from the bullfrog's sacculus. *Proc Natl Acad Sci USA* 93(18): 9527–9532.
25. Tucker T, Fettiplace R (1995) Confocal imaging of calcium microdomains and calcium extrusion in turtle hair cells. *Neuron* 15(6):1323–1335.
26. Zenisek D, Horst NK, Merrifield C, Sterling P, Matthews G (2004) Visualizing synaptic ribbons in the living cell. *J Neurosci* 24(44):9752–9759.
27. Brandt A, Striessnig J, Moser T (2003) CaV1.3 channels are essential for development and presynaptic activity of cochlear inner hair cells. *J Neurosci* 23(34):10832–10840.
28. Platzer J, et al. (2000) Congenital deafness and sinoatrial node dysfunction in mice lacking class D L-type Ca^{2+} channels. *Cell* 102(1):89–97.
29. Wong AB, et al. (2014) Developmental refinement of hair cell synapses tightens the coupling of Ca^{2+} influx to exocytosis. *EMBO J* 33(3):247–264.
30. Martinez-Dunst C, Michaels RL, Fuchs PA (1997) Release sites and calcium channels in hair cells of the chick's cochlea. *J Neurosci* 17(23):9133–9144.
31. Moreno CM, et al. (2016) Ca^{2+} entry into neurons is facilitated by cooperative gating of clustered CaV1.3 channels. *eLife* 5:e15744.
32. Kuhn S, et al. (2009) Ba^{2+} currents in inner and outer hair cells of mice lacking the voltage-dependent Ca^{2+} channel subunits beta3 or beta4. *Channels (Austin)* 3(5): 366–376.
33. Neef J, et al. (2009) The Ca^{2+} channel subunit beta2 regulates Ca^{2+} channel abundance and function in inner hair cells and is required for hearing. *J Neurosci* 29(34): 10730–10740.
34. Bock G, et al. (2011) Functional properties of a newly identified C-terminal splice variant of Cav1.3 L-type Ca^{2+} channels. *J Biol Chem* 286(49):42736–42748.
35. Tan BZ, et al. (2011) Functional characterization of alternative splicing in the C terminus of L-type CaV1.3 channels. *J Biol Chem* 286(49):42725–42735.
36. Scharinger A, et al. (2015) Cell-type-specific tuning of Cav1.3 Ca^{2+}-channels by a C-terminal automodulatory domain. *Front Cell Neurosci* 9:309.
37. Cui G, et al. (2007) Ca^{2+}-binding proteins tune Ca^{2+}-feedback to Cav1.3 channels in mouse auditory hair cells. *J Physiol* 585(Pt 3):791–803.
38. Schrauwen I, et al. (2012) A mutation in CABP2, expressed in cochlear hair cells, causes autosomal-recessive hearing impairment. *Am J Hum Genet* 91(4):636–645.
39. Yang PS, et al. (2006) Switching of Ca^{2+}-dependent inactivation of Ca(v)1.3 channels by calcium binding proteins of auditory hair cells. *J Neurosci* 26(42):10677–10689.
40. Davydova D, et al. (2014) Bassoon specifically controls presynaptic P/Q-type Ca^{2+} channels via RIM-binding protein. *Neuron* 82(1):181–194.
41. Gebhart M, et al. (2010) Modulation of Cav1.3 Ca^{2+} channel gating by Rab3 interacting molecule. *Mol Cell Neurosci* 44(3):246–259.
42. Kaeser PS, et al. (2011) RIM proteins tether Ca^{2+} channels to presynaptic active zones via a direct PDZ-domain interaction. *Cell* 144(2):282–295.
43. Jung S, et al. (2015) Rab3-interacting molecules 2α and 2β promote the abundance of voltage-gated $Ca_V1.3$ Ca^{2+} channels at hair cell active zones. *Proc Natl Acad Sci USA* 112(24):E3141–E3149.
44. Gregory FD, et al. (2011) Harmonin inhibits presynaptic Cav1.3 Ca^{2+} channels in mouse inner hair cells. *Nat Neurosci* 14(9):1109–1111.
45. Gregory FD, Pangrsic T, Calin-Jageman IE, Moser T, Lee A (2013) Harmonin enhances voltage-dependent facilitation of Cav1.3 channels and synchronous exocytosis in mouse inner hair cells. *J Physiol* 591(13):3253–3269.
46. Johnson KR, et al. (2003) Mouse models of USH1C and DFNB18: Phenotypic and molecular analyses of two new spontaneous mutations of the Ush1c gene. *Hum Mol Genet* 12(23):3075–3086.
47. Grillet N, et al. (2009) Harmonin mutations cause mechanotransduction defects in cochlear hair cells. *Neuron* 62(3):375–387.
48. Charizopoulou N, et al. (2011) Gipc3 mutations associated with audiogenic seizures and sensorineural hearing loss in mouse and human. *Nat Commun* 2:201.
49. Rehman AU, et al. (2011) Mutations of GIPC3 cause nonsyndromic hearing loss DFNB72 but not DFNB81 that also maps to chromosome 19p. *Hum Genet* 130(6): 759–765.
50. Giese AP, et al. (2012) Gipc1 has a dual role in Vangl2 trafficking and hair bundle integrity in the inner ear. *Development* 139(20):3775–3785.
51. Naccache SN, Hasson T, Horowitz A (2006) Binding of internalized receptors to the PDZ domain of GIPC/synectin recruits myosin VI to endocytic vesicles. *Proc Natl Acad Sci USA* 103(34):12735–12740.
52. Yano H, et al. (2006) BDNF-mediated neurotransmission relies upon a myosin VI motor complex. *Nat Neurosci* 9(8):1009–1018.
53. Robertson D, Paki B (2002) Role of L-type Ca^{2+} channels in transmitter release from mammalian inner hair cells. II. Single-neuron activity. *J Neurophysiol* 87(6):2734–2740.
54. Kros CJ, Ruppersberg JP, Rüsch A (1998) Expression of a potassium current in inner hair cells during development of hearing in mice. *Nature* 394(6690):281–284.
55. Johnson SL, Beurg M, Marcotti W, Fettiplace R (2011) Prestin-driven cochlear amplification is not limited by the outer hair cell membrane time constant. *Neuron* 70(6): 1143–1154.
56. Goutman JD, Glowatzki E (2011) Short-term facilitation modulates size and timing of the synaptic response at the inner hair cell ribbon synapse. *J Neurosci* 31(22): 7974–7981.
57. Cho S, Li G-L, von Gersdorff H (2011) Recovery from short-term depression and facilitation is ultrafast and Ca^{2+} dependent at auditory hair cell synapses. *J Neurosci* 31(15):5682–5692.
58. Furman AC, Kujawa SG, Liberman MC (2013) Noise-induced cochlear neuropathy is selective for fibers with low spontaneous rates. *J Neurophysiol* 110(3):577–586.
59. Hoppa MB, Lana B, Margas W, Dolphin AC, Ryan TA (2012) $\alpha 2\delta$ expression sets presynaptic calcium channel abundance and release probability. *Nature* 486(7401): 122–125.
60. Han Y, Kaeser PS, Südhof TC, Schneggenburger R (2011) RIM determines Ca^{2+} channel density and vesicle docking at the presynaptic active zone. *Neuron* 69(2):304–316.
61. Kiyonaka S, et al. (2007) RIM1 confers sustained activity and neurotransmitter vesicle anchoring to presynaptic Ca^{2+} channels. *Nat Neurosci* 10(6):691–701.
62. Zamponi GW, Striessnig J, Koschak A, Dolphin AC (2015) The physiology, pathology, and pharmacology of voltage-gated calcium channels and their future therapeutic potential. *Pharmacol Rev* 67(4):821–870.
63. Sheets L, Trapani JG, Mo W, Obholzer N, Nicolson T (2011) Ribeye is required for presynaptic Ca(V)1.3a channel localization and afferent innervation of sensory hair cells. *Development* 138(7):1309–1319.
64. Sheets L, Kindt KS, Nicolson T (2012) Presynaptic CaV1.3 channels regulate synaptic ribbon size and are required for synaptic maintenance in sensory hair cells. *J Neurosci* 32(48):17273–17286.
65. Brandt A, Khimich D, Moser T (2005) Few CaV1.3 channels regulate the exocytosis of a synaptic vesicle at the hair cell ribbon synapse. *J Neurosci* 25(50):11577–11585.
66. Pangršič T, et al. (2015) EF-hand protein Ca^{2+} buffers regulate Ca^{2+} influx and exocytosis in sensory hair cells. *Proc Natl Acad Sci USA* 112(9):E1028–E1037.
67. Ezan J, Montcouquiol M (2013) Revisiting planar cell polarity in the inner ear. *Semin Cell Dev Biol* 24(5):499–506.
68. Sienknecht UJ, Köppl C, Fritzsch B (2014) Evolution and development of hair cell polarity and efferent function in the inner ear. *Brain Behav Evol* 83(2):150–161.
69. Moser T, Beutner D (2000) Kinetics of exocytosis and endocytosis at the cochlear inner hair cell afferent synapse of the mouse. *Proc Natl Acad Sci USA* 97(2):883–888.
70. Jing Z, et al. (2013) Disruption of the presynaptic cytomatrix protein bassoon degrades ribbon anchorage, multiquantal release, and sound encoding at the hair cell afferent synapse. *J Neurosci* 33(10):4456–4467.
71. Staudt T, Lang MC, Medda R, Engelhardt J, Hell SW (2007) 2,2′-thiodiethanol: A new water soluble mounting medium for high resolution optical microscopy. *Microsc Res Tech* 70(1):1–9.